Senegalese Land Surface Change Analysis and Biophysical Parameter Estimation using NOAA AVHRR Spectral Data

Final Report

NAG-5 1068

Fred M. Vukovich

Research Triangle Institute

Research Triangle Park, NC

David L. Toll

NASA/Goddard Space Flight Center

Greenbelt, MD 20771

Ruth L. Kennard

ST Systems Corporation

Lanham, MD 20706

December 1989

DEC 21, 1989

Senegalese Land Surface Change Analysis and Biophysical Parameter Estimation using NOAA AVHRR Spectral Data

ABSTRACT

Surface biophysical estimates were derived from analysis of NOAA Advanced Very High Spectral Resolution (AVHRR) spectral data of the Senegalese area of west Africa. The derived surface parameters were of solar albedo, spectral visible and near-infrared band reflectance, spectral vegetative index, and ground temperature. Wet and dry linked AVHRR scenes from 1981 through 1985 in Senegal were analyzed for a semi-wet southerly site near Tambacounda and a predominantly dry northerly site near Podor. Related problems were studied to convert satellite derived radiance to biophysical estimates of the land surface. Problems studied were associated with sensor miscalibration, atmospheric and aerosol spatial variability, surface anisotropy of reflected radiation, narrow satellite band reflectance to broad solar band conversion, and ground emissivity correction. Of note, the middle-infrared reflectance (1.3-2.5•μm) was approximated with a visible AVHRR reflectance (0.57-0.69•μm) for improving solar albedo estimates. In addition, the spectral composition of solar irradiance (direct and diffuse radiation) between major spectral regions (i.e., ultraviolet, visible, near-infrared, and middle-infrared) was indicated to be insensitive to changes in the clear sky atmospheric optical depth in the narrow band to solar band conversion procedure.

Solar albedo derived estimates for both sites were indicated not to change markedly with significant antecedent precipitation events or correspondingly from increases in green leaf vegetation density. The bright soil/substrate contributed to a high albedo for the dry related scenes, whereas the high

internal leaf reflectance in green vegetation canopies in the near-infrared contributed to high solar albedo for the wet related scenes. Furthermore, the relationship between solar albedo and ground temperature was poor, indicating the solar albedo has little control of the ground temperature. NDVI and the derived visible reflectance were more sensitive to antecedent rainfall amounts and green vegetation changes than were near-infrared changes. The information in the NDVI related to green leaf density changes primarily was from the visible reflectance. The contribution of the near-infrared reflectance to explaining green vegetation is largely reduced when there is a bright substrate.

INTRODUCTION

The western sub-Saharan region has over the last decade undergone periods of severe drought followed by periods of near-average rainfall (Motha et al. 1980 and Nicholson 1985). Nicholson (1983) reports there is a strong persistency to the sub-Saharan drought differing markedly in duration in comparison to other regional droughts. The exact causes for this prolonged drought are unclear, but some research results have linked its prolonged nature to land surface- atmosphere interactions (Charney, et al. 1977 and Sud and Smith 1985), to atmospheric circulation changes causing a displacement southward of the subtropical high (Lamb 1978), and to a weakened zonal easterly air jet flow (Kanamitsu and Krishnamurti 1978).

Analysis of the polar orbiting NOAA Advanced Very High Resolution Radiometer (AVHRR) spectral data may provide a means to study regional land surface changes associated with drought and anthropogenic activities and provide further insight to surface atmosphere interaction. The NOAA-7 and NOAA-9 polar orbiting satellites both have a daily early afternoon overpass conducive to monitoring land surface change. Furthermore, the high temporal resolution of the satellite data increases the probability for obtaining cloud free dates. In addition, the AVHRR has a 1.1 km ground field of view at nadir and has two spectral bands in the optical region and three in the thermal infrared region.

However, the extraction of biophysical parameters of the land surface from the AVHRR directional and spectral radiance is associated with numerous difficulties. The lack of an on-board calibrator for the AVHRR shortwave bands 1 and 2 detectors, coupled with a reported degradation in the spectral response (Frouin and Gautier 1987 and Holben et al. 1989) confounds the extraction of accurate radiance data for surface reflectance derivations and comparisons between dates. The directional only viewing of surface anisotropic reflected surface radiation may lead to an uncertainty when attempting to estimate a hemispherical exitance (e.g., Kimes et al. 1985). In

addition, the narrow band passes of the AVHRR cover only a small proportion of the total incident solar radiation, causing an inaccurate estimation of a total incident solar band reflectance (Toll 1989). The heterogeneous ground surface emissivity complicates the estimation of a land surface temperature (Becker 1987). In addition, the extreme high water vapor and aerosol loading in the sub-Saharan is associated with a high spatial and temporal variability (D'Almeida 1986), making atmospheric corrections difficult. Other remote sensing problems arise from geometric misregistration of the image data (Billingsley et al. 1983), sensor autocorrelation of the spectral data (Labovitz et al. 1982), and spectral resolution changes between and among sensors (Malila et al. 1987).

The primary objective of the study is to use AVHRR derived spectral data to evaluate land surface changes and to provide biophysical information derived from the satellite radiance to examine land surface-climatology interactions. To characterize the landscape, surface derived estimates of solar albedo, spectral vegetation index and ground temperature are extracted from the AVHRR spectral data. The solar albedo is an estimate of the spectrally integrated hemispherical exitance reflected from the incident solar irradiance (direct plus diffuse) at the surface. The solar albedo may be used to estimate the amount of absorbed energy at the surface for studying land-air energy interactions (e.g., Charney et al. 1977) and may be used to document land surface feature change (e.g., Robinove 1981). Also computed is the visible and near-infrared reflectivity, since when computing the solar albedo, spectrally dependent information is frequently lost (Dickinson 1983). A normalized difference vegetation index (NDVI) maximizing green vegetative related variations is estimated from visible and near-infrared derived reflectance (Tucker 1979). Goward et al. (1986) indicates a seasonal integration over the growing season for the NDVI gives an estimate of green vegetation density with a strong link to biome net primary productivity. Similarly, Tucker et al. (1986) and Shibayama and Askiyama (1989) report a near-infrared and visible spectral vegetative index

may be used to estimate standing green biomass. However, Sellers (1987) indicates for dark soil substrates the NDVI is better related to minimum canopy resistance and to vegetative net primary productivity. Ground temperature is estimated for assessing surface heating effects relative to spectral reflectance and rainfall amounts, and may be used in subsequent investigations to estimate surface heat energy fluxes. Surface meteorological data of the western sub-Saharan for Tambacounda and Podor (available from the NOAA National Climate Data Center, NCDC) were used to report climatic conditions and to describe the state of the atmosphere (e.g., temperature, rain, aerosol loading, wind, and clouds) for the time of the satellite overpass.

STUDY SITE

The area selected for study is the Senegalese area in the sub-Saharan encompassing two ecological areas from north to south, the Sahel (averaging 100-400 mm of precipitation) and the Soudan (400-800•mm) (Nicholson 1983). The study region area is diverse because of a steep south to north precipitation gradient, with mean annual isohyets occurring parallel to equal lines of latitude. The vegetation is largely steppe, with changes to desert in the north and changes to savannah in the the south (Monad 1986). The area has extensive pastoral lands, largely from insufficient rainfall to support agriculture. Man induced effects from overgrazing of livestock and gathering of firewood has compounded the environmental effects from drought. Justice and Hiernauz (1986) report these changes have led to an overall lower net primary productivity as derived through analysis of NOAA AVHRR spectral data. Tucker et al. (1986) notes the resiliency of the land with an increasing net primary productivity for much of the Sahelian region following a period in 1985 of increased rainfall. For this effort, a dry northerly site near Podor (16°30'•N 14°24'•W) and a semi-dry/wet southerly site near Tambacounda (13°47'N 13°40'•W) were selected for analyses.

APPROACH AND ANALYSES FOR SURFACE PARAMETER DERIVATION

Shortwave Radiometric Calibration

There is no on-board calibrator for the AVHRR shortwave visible and near-infrared bands. Instead a vicarious calibration technique is typically used to determine post-launch calibration changes. Frouin and Gautier (1987) estimates a 15% post-launch decrease in radiometric gain for the shortwave NOAA-7 AVHRR bands. The decrease was based on field and atmospheric recorded observations versus AVHRR derived spectra of White Sands, New Mexico. Holben et al. (1989a) through analysis of Saharan derived reflectivities indicates a gain change to 20% for both NOAA-7 and NOAA-9 shortwave bands. Further, they documented a time varying gain change worsening with time. The Holben et al. (1989) radiometric adjustments (a') were used to correct the AVHRR spectral data.

$$\rho_{cal} = DV*(a/a') - b_o \qquad (1)$$

ρ_{cal} - calibrated exoatmospheric reflectance
DV - uncalibrated digital value from computer tape
a - NOAA prelaunch calibration (gain) coefficient
a' - gain prelaunch modifier from Holben and Kaufman (1989)
b_o - NOAA calibration (offset) coefficient

The NOAA AVHRR calibrations to exoatmospheric reflectance were converted to radiance for use in atmospheric corrections for deriving a surface reflectance.

$$L_{sat} = \rho_{cal}/K * E \qquad (2)$$

L_{sat} - Satellite derived irradiance ($W \bullet m^{-2} \bullet sr^{-1}$)

K - Earth - Sun distance correction factor (Sturm 1981)

E - Solar irradiance ($W \bullet m^{-2} \bullet sr^{-1}$)

The exoatmospheric derived calibrations were converted from the NOAA provided (Thekaekara 1973) solar irradiance data to that of the more widely recommended data of Neckel and Labs (1984). Table 1 shows the conversion factors with the effective solar irradiance comparisons for NOAA AVHRR reflective wavebands (also discussed in Price 1987). For the AVHRR visible band there is a change in reflectance to 5.9%, for the near-infrared band there is a change to 2.3%.

Table 2 provides data on the visible and near-infrared exoatmospheric derived reflectance with and without the post-launch calibration. The 1981-1984 AVHRR scenes were collected from NOAA-7 and the 1985 scenes from NOAA-9. To illustrate the significance of the calibration conversion the NDVI is also given, since the NDVI magnifies the visible to near-infrared difference. The average difference is pronounced for the NDVI varies from 9.2% to 3.5% for the visible reflectance and to 6.1% for the near-infrared reflectance. Hence, radiometric calibration changes alone may mask out any real surface reflectance change. Furthermore, the substantial increases in spectral reflectance and NDVI from radiometric calibration changes alone are time varying, increasing with time from launch.

Image Rectification and Cloud Cover Removal

Initially, a master scene was registered to surface maps using ground control points. All subsequent processed scenes were corrected for panoramic distortion and mapped to the master scene using one tie point. The image data were mapped using a Lambert Conformal map projection and then compared to the master scene for analysis of misregistration error.

Overall residual mean square errors between processed scenes were one pixel or less.

Cloud contaminated pixels were removed by determining a thresholded via an image display terminal through selecting the darkest visible (band 1) and warmest thermal infrared (band•4) spectral value occurring over clouds. A subsequent step was implemented of labeling areas of high spatial variability as cloud contaminated (Gutman 1987).

Shortwave Atmospheric Correction

The relationship between a Lambertian surface reflectance (ρ_{sur}) and the upward spectral radiance (L_{sat}) measured by the satellite (Chandrasekhar 1960) is given next with a spectral dependence (λ) implied.

$$L_{sat} = L_o + (F_{sur}/\pi) * (T*\rho_{sur}/(1-s*\rho_{sur})) \qquad (3)$$

L_{sat} - satellite calibrated radiance ($W \cdot m^{-2}\ sr^{-1}$)
L_o - atmosphere to satellite path radiance ($W \cdot m^{-2}\ sr^{-1}$)
F_{sur} - surface solar irradiance ($W \cdot m^{-2}$)
T - surface to satellite total transmittance (direct + diffuse)
s - atmosphere to surface counter-reflectance
ρ_{sur} - isotropic surface reflectance

The measured satellite radiance for bands 1 and 2 were converted to reflectance using the relationship given next.

$$\rho_{sur} = L_{sat} - L_o / (T'*F_o(1/\pi) + s(L_{sat}-L_o) \qquad (4)$$

T' - Total downwelling times upwelling atmosphere transmittance (Ahmad and Fraser 1982)

The L_{sat} was derived from the NOAA AVHRR calibrated radiance (Equation 2). The atmospheric correction was developed using the radiative transfer model described by Ahmad and Fraser (1982). The model incorporates a multiple scatter radiative transfer procedure after Dave (1972) with inclusion of polarization effects. The model assumes a spherical aerosol for solution using Mie theory. In addition, the model assumes a horizontally homogeneous atmosphere bounded by a Lambertian reflecting surface. The atmosphere is assumed cloud free. The index of refraction is assumed to be m = 1.54-0.003i. The real number of 1.54 is considered typical of the sub-Saharan (e.g., Carlson and Caverly 1977) and the imaginary part at 0.003 is less known but was selected by inspecting results by Patterson et al. (1977) and a personal communication from Holben (1988. The size distribution of the aerosols was represented by a power law distribution. Gaseous absorption attributes were estimated using the optical properties specified in the tropical model (15°N) from McClatchey et al. (1971). The model includes estimates for pressure, temperature, aerosols, water vapor and ozone. The pressure, temperature and water vapor vertical distributions were normalized for conditions at the time of the satellite overpass for Tambacounda and Podor by using the near hourly surface meteorological data from NCDC (i.e., ambient air temperature, surface atmospheric pressure and dew point temperature). A strong relationship of the surface recorded water vapor amount (via the surface dew point temperature) to the vertical atmospheric water content was reported by Mohamed and Frangi (1983) for atmospheric conditions near Niamey, Niger. A linear comparison of surface dew point temperature versus atmospheric precipitable water indicates a linear correlation coefficient of r = 0.89.

$$\ln Ps = 0.0581 Td + 0.23 \qquad (5)$$

Ps - precipitable water (cm)

Td - dew point temperature (C^{o})

Hence, using the surface dew point temperature from NCDC to adjust the atmospheric water vapor model ($15^{o}N$) of McClatchey et al. (1971) was considered to provide a reasonable estimate.

Water vapor and ozone optical depths for input to the radiative transfer model of Ahmad and Fraser (1982) were derived from modification of the vertical gaseous distributions input to the LOWTRAN-6 atmospheric radiative transfer model (Kneizys et al. 1983). The ozone atmospheric optical depth derived using Lowtran-6 was used in the Ahmad and Fraser model. However, Holben and Eck (1989) indicates that atmospheric water vapor in the sub-Saharan is high and varies significantly temporally and spatially. Hence, the tropical model from McClatchey used in Lowtran-6 was modified to represent the atmospheric water vapor for the study sites at the time of the satellite overpass. Mohamed and Frangi (1983) reports through analysis of data near Niamey, Niger, that water vapor optical depth estimates have a strong linear relationship ($r = 0.89$) between the surface dew point temperature and the atmospheric precipitable water.

Water vapor optical depth estimates derived for Tambacounda and Podor are plotted in Figures 1 and 2 with monthly averaged dew point temperature. The magnitude of the water vapor optical depth is high, peaking at values above 0.15 during the rainy season and above 0.08 during the dry season. Inspection of the monthly dew point temperatures indicates that only the winter months are associated with a low atmospheric water vapor. Although Tambacounda receives considerable more rainfall than Podor, the atmospheric water vapor recordings are comparable.

The aerosol optical depth in the western sub-Saharan may be extremely high with optical depths averaging over one during the spring-summer months when there is high solar insolation (D'Almeida 1987 and Holben et al. 1989b). The atmospheric aerosol density distribution (McClatchey et al.

1971) was represented through specification of an aerosol optical depth. Aerosol optical depths were estimated using two different approaches. Two approaches were evaluated because of the complexity in estimating an aerosol optical depth without concurrent field measurements and the high temporal and spatial variability reported by D'Almeida and Holben et al. (1989b).

In the first approach, the aerosol optical depth network of Holben et al. (1989b) for Agadez, Gao, Sevare, and Bamako was seasonally and latitudinally adjusted to estimate optical depths for Podor and Tambacounda (Table 3). They were converted to an AVHRR band•1 and band 2 aerosol optical depth ($\tau_{a,\lambda}$) represented by the wavelengths 0.639•μm and 0.845•μm (Fraser et al. 1987).

$$\log \tau_{a,\lambda} = \alpha * \log(0.875/\lambda) + \log(\tau'.875) \qquad (6)$$

α - Angstrom wavelength exponent

λ - wavelength, used 0.639 μm for band-1
and 0.845 μm for band-2

The Angstrom turbidity coefficient (α) then was estimated from an empirical approximation of the wavelength exponent versus the aerosol optical depth through analysis of data from the west African Sun photometer network of Holben et al. (1989b).

$$\alpha = 0.5189 - 0.4433\, \tau'.875 \qquad (7)$$

In the second approach, an aerosol optical depth was derived from a surface meteorological range via an observer recorded visibility. The visibility was obtained for Podor and Tambacounda at a time near the satellite overpass. The observer visibility (V_{obs}) was converted to a meteorological

range (V) through multiplication by 1.3 ($V = V_{obs} * 1.3(\pm 0.3)$) (Kneizys et al. 1983). The horizontal range was converted to an aerosol optical depth using an empirically based transformation ($r = 0.96$) derived by D'Almeida (1986). D'Almeida analyzed west sub-Saharan aerosols in Assekrem, Algeria and Boutilimit, Mauritania.

$$\beta = 2.26\ (V)^{-.73} \qquad (8)$$

β - Angstrom turbidity coefficient

The Angstrom attenuation coefficient (β) then was converted to an aerosol optical depth (τ'_a)

$$\tau'_a = \beta\lambda^{-\alpha} \qquad (9)$$

The Angstrom wavelength exponent which is a function of the size distribution of the aerosols was estimated through an iterative procedure using Equation•6 with an initial estimate for the aerosol optical depth.

When using the surface derived visibility, variations in the aerosol scale height may yield an incorrect optical depth estimate. Mohamed and Frangi (1986) developed a procedure to adjust the aerosol optical depth obtained from surface visibility data, through estimation of the height of the planetary boundary layer (pbl). However, the vertical resolution of the temperature profile for Tambacounda (sounder data from NOAA NCDC) was too coarse for determining the pbl. Comparisons of the observer visibility data versus the aerosol optical depth using the Sun photometer derived data for Bamako, Mali (Holben et al. 1989b), yielded a correlation coefficient (r) of 0.82 (Figure 3). Hence, there is an indication of a similar trend between surface visibility and atmospheric aerosol optical depth.

Aerosol optical depth estimates for the two approaches with the computed surface reflectance is compared for Tambacounda (Table 4). Overall, aerosol optical depth estimates are lower when using the observer visibilities versus the adjusted optical depths from the Holben et al. (1989b) Sun photometer network. However, Holben et al. (1989b) indicates the spatial variability of aerosols is high and hence using spatial extrapolations between locations may introduce significant error. Hence, the differences may be partially attributed to site specific and hourly derived visibility estimates coinciding with the satellite overpass. This is in comparison to the monthly averaged and latitudinally adjusted optical depths from the Sun photometer network. An additional explanation is that the dates selected for processing were screened initially for ordering high contrast images (an indicator of decreased atmospheric haze and cloudiness), yielding a lower aerosol optical depth estimate with a lower derived surface reflectance. The lower surface reflectance is from a reduced atmospheric transmissivity and to a lesser extent from both a lower atmosphere to satellite and surface reflectance. Furthermore, the reflectances derived with the observer visibiltiy related approach are similar to the satellite derived surface reflectances of the sub-Saharan as reported by Pinty and Szechwah (1985). Hence, surface derived reflectances based on the atmospheric optical depth were estimated via the observer visibility related approach.

Surface Anisotropy

The estimation of a surface, solar albedo using satellite radiance (Equation 4) assumes an isotropic reflecting surface. However, there are several illumination and viewing geometry conditions where a directional derived reflectance may misrepresent a hemispherical reflectance by over 50% (Kimes et al. 1985). On the other hand, the assumption of isotropy for visible and near-infrared wavelengths is adequate for many surface covers between the solar zenith angles 20^{o} to 40^{o} (Kimes and Sellers 1987 and Middleton et

al. 1987). For many of the scenes processed, the Sun zenith angles were within this illumination range of 20° to 40°. For those scenes associated with Sun zenith angles greater than 40° (there were no scenes associated with Sun zenith angles less than 20°), a hemispherical reflectance conversion model was evaluated.

An empirical transformation by Middleton et al. (1987) to convert directional reflectance to a hemispherical reflectance for a range of semi-arid to arid surface covers in North America was tested. However, the approach was considered inappropriate due to a large discontinuity between the converted reflectances and the isotropic assumed reflectances for Sun zenith angles at approximately 40°. The highest Sun zenith angle is for the Oct. 25, 1985 AVHRR scene with an angle of 50.8 ° for Tambacounda and 51.3 % for Podor. Kimes and Sellers (1987) indicates an anisotropic related error of 5% visible and 7% near-IR for steppe-grassland with a 50° Sun zenith angle. Steppe-grassland is a common surface cover in the study site. Based on these results, the assumption of surface reflectance isotropy was made for all the scenes processed, even though a larger hemispheric reflectance error associated with scenes having large Sun zenith angles is possible.

AVHRR Narrow Band to Solar Band Reflectance Conversion

A model by Brest and Goward (1987) for converting Landsat Multispectral (MSS) derived reflectance to solar albedo was further developed and modified for converting the visible and near-infrared band 1 and 2 derived reflectance to a solar albedo.

$$\rho solar = \rho vis * k vis + \rho nir * k nir + \rho smir * k smir \qquad (10)$$

$\rho solar$ - solar albedo

$\rho spec$ - derived surface reflectance for the spectral regions (visible (0.38-0.72•μm), near-infrared (0.72-1.30•μm)

and shortwave middle-infrared (1.30-3.0•μm)

k - relative proportion of surface, solar irradiance by spectral region

For a vegetative canopy there are four major spectral regions in the solar region with similar optical properties (Gausman 1985). The four spectral regions are ultraviolet (0.30-0.38•μm), visible (0.38-0.72•μm), near-infrared (0.72-1.30•μm) and shortwave middle-infrared (1.30-3.0•μm). Figure 4 gives a representative example of the optical properties for a green leaf. In the visible region, plant pigments chlorophyll, carotenes and xanthophyll absorb much of the solar radiation. Leaf absorption is the lowest for green light (0.45•μm) with an absorptance approximately 5% units less than for blue or red light. The near-infrared radiation for plants is characterized by a low absorption and high reflectance and transmittance that is largely determined by internal leaf structure from intercellular refractive discontinuities (Grant•1987). The shortwave middle-infrared (1.30-3.0•μm) is characterized by liquid water absorption peaking at 1.45•μm and 1.94•μm and also is affected by leaf intercellular refractive discontinuities (Gausman 1985). In the ultraviolet region there is no transmittance with approximately 9% reflectance and 91% absorptance.

The percent of the solar radiation sensed by the AVHRR bands 1 & 2 bandpass for NOAA-7 and NOAA-9 at the top and the bottom of the atmosphere is given in Table 5. To estimate the atmosphere radiative transfer, a mid-latitude data set from Dave' (1978) was evaluated that modeled an atmosphere with gaseous absorption and a low aerosol loading. The small proportion of solar radiation that is represented by the AVHRR (50% and less), indicates a potential problem for estimating a broad band, solar albedo.

Analysis of high spectral resolution field data by Toll (1989) indicates AVHRR band 1 and band 2 reflectance may be used to estimate both a total visible (0.38-0.72•μm) and total near-infrared (0.73-1.30•μm) reflectance

because of the high intra-region correlation. The combined visible and near-infrared regions represents approximately 85% of the total solar radiation at the surface with the remaining 15% in the shortwave middle-infrared (10%) and ultraviolet (5%) regions. However, a linear transformation is required when estimating a total visible and near-infrared reflectance (Toll 1989). Errors to 20% may be obtained when using an AVHRR visible (e.g., 0.57-0.69•μm) or near-infrared (0.71-0.98•μm) reflectance to directly estimate a total visible (0.37-0.72•μm) or near-infrared (0.73-1.30•μm) reflectance without a linear transformation. The derived visible reflectance was used to represent an ultraviolet reflectance with only a small reduction in accuracy accounting for less than 5% of the surface solar radiation for ultraviolet light. Toll (1989) indicates a difference of less than 1% when using a visible derived reflectance to represent an ultraviolet reflectance for several illumination and canopy conditions. Therefore, the ultraviolet spectral region reflectance in Equation 10 is assumed to be represented by the visible reflectance.

The absence of a shortwave middle-infrared detector on the AVHRR may introduce errors to over 20% in comparison to using a near-infrared reflectance (0.72-1.30•μm) to represent a total shortwave IR region (0.72-1.30•μm) (Toll 1989). Brest and Goward (1987) used 0.5 times the near-infrared reflectance to estimate a shortwave middle-infrared reflectance. However, the near-infrared optical properties for green vegetation are markedly different than for the middle-infrared with a substantially higher absorptance of solar radiation (three to eight times higher green leaf absorptance) in the middle-infrared (Figure 4).

Landsat Thematic Mapper satellite derived reflectance in the visible and near-infrared regions were compared against a middle infrared reflectance for the purpose of estimating a middle-infrared reflectance from the AVHRR sensing in only the visible and near-IR region of the solar band. The TM has three bands in the visible, one in the near-infrared, and two in the middle-infrared. The TM spectral data were radiometrically calibrated to radiance, corrected for Sun zenith angle and Earth-Sun distance, and converted to an

exoatmospheric reflectance using Neckel and Labs (1984) solar irradiance data. The available TM digital scenes in western Africa for analysis was low due to few scene acquisitions, a high cloud cover, and a low satellite overpass cycle (i.e., once every 18 days). The Landsat Thematic Mapper (TM) data for three dates were analyzed. The three Landsat TM scenes selected for analysis were on August 21, 1984 (17°57'N 8°0'E scene center point) September 24, 1984 (15°55'N 14°•55'W), and October 23, 1986 (14°27'N 16°44'W). Regression analysis results between derived spectral reflectances (i.e, band combinations between the visible and near-infrared versus the middle-infrared spectral regions) are given in Table•6. To reduce spatial autocorrelation effects and hence statistical interdependence, the TM pixel data were sampled by at least every tenth pixel in both the across and along scan line directions (Labovitz et al. 1982). An estimated exoatmopsheric NDVI is also included for an indication of green leaf vegetative density.

Overall the relationship of the visible and near-infrared reflectance to the middle-infrared reflectance is strong, with a multiple regression coefficient (R) of 0.68 and higher (Table 6). Except for the 1984 scene ($r = -0.05$) the linear relationship of the near-infrared to shortwave middle-infrared reflectance relationship is strong ($r = 0.77$ and $r = 0.84$). In comparison the linear relationship of a middle-infrared to a visible reflectance is strong for all three dates is high ($0.74 < r < .94$). A reason for the closer link between visible and middle-infrared over the link between near-infrared and middle-infrared may be attributed to a closer similarity of leaf absorptance related effects between regions. Specifically the plant pigments (primarily chlorophyll) absorb radiation in the visible and canopy water absorb radiation in the middle-infrared. However, the strength of the visible to the middle-infrared relationship is not significantly improved by the addition of NDVI in the ANOVA (Table 6). Based on the TM related and examination of the spectra published in Bowker et al. (1985), we derived a middle-ir reflectance from the

AVHRR spectral data by multiplying the AVHRR visible reflectance by 1.5 (i.e., $\rho_{smir} = \rho_{vis} * 1.5$).

Table 7 gives the percentage of solar irradiance incident at the surface in terms of diffuse, direct and global (direct + diffuse) radiation integrated over the four major spectral regions. The relative proportion of surface radiation by spectral region gives the weighting for the solar band estimation in Equation 9. The atmospheric radiative transfer data of Dave' (1978) using three mid-latitude models (Model 2 -atmospheric gaseous absorption with no aerosols, Model 3 - gaseous absorption with a low aerosol loading, and Model 4 - gaseous absorption with a high aerosol loading) at selected Sun zenith angles was used to examine the spectral region variability. The global radiation percentages given in Table 7 are the spectral region solar irradiance coefficients (i.e., k) in Equation (10). As expected for both an increasing Sun zenith angle (i.e.,•0 to 70 θ_S) and an increasing aerosol loading (Model 2 to 3 to 4), there is increased scattering, producing less direct radiation and more diffuse radiation. For direct radiation, there is proportionally less energy in the ultraviolet and visible regions with a shift of energy to the near-ir and middle-ir wavelengths. However, as evident by the small changes in the global radiation proportions between illumination and atmospheric haze conditions, there is a strong compensating effect of an increased diffuse radiation from forward Mie scattering adding to the reduced direct radiation. Differences between values in the visible, near-infrared and middle-infrared have a range of less than 3%. Hence, examination of results indicates a single average set of spectral region proportions for the global radiation may be used in Equation (9). The spectral proportions used were from the 45^{o} Sun zenith angle for the heavy aerosol model of 0.046 ultraviolet, 0.471 visible, 0.378 near-IR, and 0.099 middle-IR.

Surface Temperature Estimation

The calibrated brightness temperature for bands 4 and 5 (NOAA 1981) are used in a split window technique to correct for atmospheric absorption effects (Strong and McClain 1984). The procedure was developed using sea surface temperatures, assuming a constant sea-surface emissivity.

$$T_7 = 3.6125*T_{B-11} - 2.5779*T_{B-12} - 10.05 \quad (11)$$

$$T_9 = 3.6446*T_{B-11} - 2.6616*T_{B-12} + 5.2 \quad (12)$$

T - surface temperature corrected for atmospheric effects for NOAA-7 and NOAA-9 respectively

T_{B-11} - AVHRR band 4 brightness temperature

T_{B-12} - AVHRR band 5 brightness temperature

The root mean square of AVHRR derived surface temperature versus drifting buoy readings is reported at 0.6°C (Strong and McClain 1984). Unfortunately, small differences between the sea-surface emissivity and the ground emissivity may lead to large derived ground temperature errors. For land surfaces, Cooper and Asrar (1989) indicate the NOAA split window technique provides land surface temperatures within $\pm$ 3°C of in•situ measurements. To adjust the split window derived surface temperatures for land surfaces with an emissivity different than that for water the following relationship from Vukovich et al. (1987) was used.

$$T_g = T_c(\epsilon_s/\epsilon_g)^{1/n} \quad (13)$$

T_g - ground temperature

ϵ_s - sea surface emissivity

ϵ_g - ground emissivity

n - temperature exponent ($I = \epsilon T^n$)

T_C - temperature from split window procedure

The value of n, according to Price (1985), is approximately 4.5. A sea surface emissivity (ϵ_S) of 0.99 was used. The ground emissivity (ϵ_g) for the study site ranges from 0.93 in the arid region to the north to 0.97 in the more densely vegetated area to the south (Wolfe and Zissis 1978). The emissivity is approximately proportional to the amount of vegetation and surface water. We assumed the derived spectral vegetation index, ranging between 0 and 0.6 was linearly related to the surface emissivity. Hence, a ground emissivity was scaled by the NDVI using the equation given next.

$$\epsilon_g = 0.93 + (NDVI * 0.0667) \qquad (14)$$

ANALYSIS REPORT

Monthly mean precipitation, surface air and dew-point temperature, and the height of the lifting condensation level (LCL) relative to the surface are given in Figures 5 and 6 for Tambacounda and Podor. For both Podor and Tambacounda, the rainy seasons occur during midsummer and are associated with the migration of the intertropical convergence zone and the accompanying horizontal flux of moisture in the lower levels. The initiation of the rainy season has occurred as early as April and terminated as late as October. Though the amount of atmospheric moisture is about the same at the two locations, the rainfall is greater at Tambacounda, which is south of Podor. At both locations, the influx of moisture produces a lower LCL height which increases the potential for convective clouds and precipitation, since less work will be required, under this condition, to produce clouds and precipitation. At Tambacounda, the LCL height is lower than that at Podor apparently due to the lower surface air temperature, which is brought about by the greater cloudiness at Tambacounda (i.e., greater precipitation

amounts) since the moisture is about the same. This factor may be attributed to a feedback mechanism since the potential for cloudiness and precipitation becomes greater at Tambacounda with a lower LCL height.

Tables 8 and 9 provide the resultant radiation parameters for the case studies over the period 1981 to 1985. Radiation parameters presented in the table represent a 10 x 10 pixel area average. The standard deviation over the area is also presented in Tables 8 and 9 and these are the values in the parentheses. Tables 8 and 9 also contain values representing two to four week antecedent precipitation amount. It can be seen that approximately 50% of the cases had antecedent precipitation, and the remaining 50% did not.

Inspection of Table 10 indicates that the average visible and near-infrared reflectance, albedo, and ground temperature at Podor were larger than that at Tambacounda. This fact is likely due to the greater amount and density of vegetation at Tambacounda (as reflected by the larger value of the NDVI at Tambacounda). During the dry period (no antecedent precipitation), the visible reflectance and the ground temperature are high, and the NDVI and near-infrared reflectance are low compared to the average values during the wet period (existing antecedent precipitation), which is indicative of a bright substrate having little or no green vegetation during the dry period. The range for the visible and near-infrared reflectance, the NDVI, and the ground temperature between the wet and dry periods for Tambacounda are larger than that at Podor, reflecting a greater variance in vegetation from dry to wet periods at Tambacounda. Within the limits of accuracy of computations, the results in Table 10 suggest that there was no variation in the albedo between the dry and wet period. This largely was due to the compensating effect of the visible reflectance and near-infrared IR reflectance between dry and wet periods. The decrease in visible reflectance during the dry to wet period is from an increase in vegetation with an increased absorption from leaf pigments, primarily chlorophyll. On the other hand, for near-infrared radiation there is a higher reflectance with increasing vegetation due to

increase scattering from high intercellular refractive discontinuities occurring within a leaf.

However, the results in Table 10 are partly biased by the fact that the precipitation amounts in some cases were very small or occurred early in the rainy season before substantial vegetation was produced. Table 11 provides average values for the visible reflectance, the near-infrared reflectance, and the albedo at Tambacounda and Podor as a function of the vegetation. Substantial vegetation was considered to exist if the NDVI were greater than or equal to 0.2 in both cases. The results at Tambacounda indicate changes in the solar albedo as a result of the vegetation was not substantial. Again this was due to the compensating effects of the reflectance of visible and near-infrared bands. At Podor where substantial vegetation to the existence of some vegetation. The vegetation that was produced apparently was not sufficient to affect the near-infrared reflectance, but had a significant influence on the visible reflectance. In either case, the presence or absence of vegetation did not substantially change the albedo from its overall mean value (compare the overall mean values of the albedo in Table 10 with the albedo values associated with the NDVI in Table 11). This suggests that the underlying ground conditions or substrate has a controlling influence on the albedo at these two locations, and unless major changes occur in the background conditions, major changes in the albedo due to the presence or absence of vegetatio/precipitation does not occur.

Trends in the behavior of the radiation parameters shown in the correlation parameter matrixes presented in Tables 12 and 13. The NDVI is strongly and inversely correlated with the visible reflectance, but shows very little relationship to the near-infrared reflectance. The inverse relationship between the NDVI and the visible reflectance is caused by the increased absorption in the visible by the vegetation, having a higher chlorophyll pigment concentration, that is produced during the rainy season. In the dry season, the highly reflective substrate controls surface radiation processes. Since vegetation should be correlated with precipitation, the NDVI and the

visible reflection should be reasonably correlated with precipitation also, for the reasons given above. However, the correlation between the near-infared reflection and precipitation was low. In the case of Tambacounda, if the date with no precipitation were removed from the data set, the correlation increased markedly ($r = .906$), which indicated that the spectral variation from then non-green background was highly variable as indicated by the data themselves, ($0.35 \leq \rho_{nir} \leq 0.60$), contributing to the scatter and poor relationship to not only the precipitation but also the NDVI.

The NDVI was reasonably well correlated with the albedo at Podor, but not so well correlated with the albedo at Tambacounda. This is undoubtedly because there was some variation in the albedo with vegetation/precipitation at Podor, whereas little to no such variation existed at Tambacounda. The relationship of ground temperature to the antecedent rainfall and the NDVI (vegetation) was, for the most part, moderate. However the data would suggest that the relationship should be more substantial, especially at Tambacounda. At Tambacounda and for the NDVI, a natural logarithm transformation improved the linear correlation from $r = -0.67$ to $r = -0.72$. The correlation between ground temperature and solar albedo was very low, suggesting that the albedo has little control on the ground temperature. The ground temperatures more than likely are controlled by the presence or absence of clouds, vegetation, and moisture.

SUMMARY AND CONCLUSIONS

NOAA AVHRR spectral data were converted to biophysical estimates of surface parameters. The estimated parameters were normalized difference vegetation index, solar albedo, spectral visible and near-infrared reflectance, and ground temperature. Several problems affecting the derivation of surface biophysical parameters were examined. Correction for post-launch radiometric calibration and atmospheric correction in a multiple scattering atmosphere were indicated to substantially affect the derived surface

reflectance. To correct for atmospheric effects when deriving a surface spectral reflectance, surface horizontal visibility (to estimate an aerosol optical depth), and surface dew point temperature (to estimate a water vapor optical depth) were used in a radiative transfer model including multiple scattering, bounded by an isotropic reflecting ground surface. The range of Sun zenith angles for the study minimized much of anisotropic variation affecting the derived surface reflectances. The narrow band visible and near-infrared derived reflectances were used to estimate a solar albedo. In the transformation procedure a middle-infrared reflectance was estimated by multiplying the visible reflectance by 1.5. The relationship between visible and middle-infrared reflectance for a vegetative surface is from a related absorption of solar radiation by plant pigments in the visible and by leaf water in the middle-infrared, coupled with leaf internal scattering, likely form from refractive index discontinuities. The near-infrared radiation interaction in a leaf is typically either transmitted or reflected with little to no absorption. In the conversion model, the spectral composition of the solar irradiance (ultraviolet, visible, near-infrared, and middle-infrared) was shown to be insensitive to clear sky atmospheric optical depth, thereby improving on the estimation of a solar albedo. NDVI estimates from the visible and near-infrared ground reflectance were used to adjust the split-window derived sea surface temperature to a land surface temperature.

The estimated biophysical parameters were obtained for 17 dates for two sites in Senegalese area of the western sub-Saharan. The dates covered spectral data from the years 1981-1985, representing both dry and wet periods. Satellite derived parameters were compared to surface meteorological data of precipitation, air temperature and atmospheric moisture. Solar albedo estimates did not change markedly with antecedent precipitation events or green leaf vegetation changes. The bright soil/substrate contributed to a high albedo for the dry related scenes, whereas the high internal leaf reflectance in green vegetation canopies in the near-infrared contributed to high solar albedo for the wet scenes.

Furthermore, the relationship between solar albedo and ground temperature was poor, indicating the solar albedo has little control of the ground temperature. NDVI and the derived visible reflectance were more sensitive to green vegetation changes than were near-infrared changes as indicated through comparisons with antecedent precipitation.

REFERENCES

Ahmad, Z. and R. Fraser, 1982. An iterative radiative transfer code for ocean-atmosphere, J. Atmos. Sci., 39(3):656-665.

Becker, F.,1987. The impact of spectral emissivity on the measurement of land surface temperature from a satellite, Int. J. Remote Sensing, 8:1509-1522.

Bowker, D., R. Davis, D. Mycick, K. Stacy, and W. Ives, 1985. Spectral reflectance of natural targets, Langley Research Center, Hampton, VA.

Billingsley, F., P. Anuta, J. Carr, C. McGillen, D. Smith and T. Straud, 1983. Data processing and reprocessing, in Manual of Remote Sensing, Vol 1, eds., R. Colwell, D. Simonett and F. Ulaby, American Society of Photogrammetry, Falls Church, VA.

Brest, C. and S. Goward, 1987. Deriving surface albedo measurement from narrow band satellite data, Int. J. Remote Sensing, xx

Carlson, T. and R. Caverly, 1977. Radiative characteristics of Saharan dusts at solar wavelengths, J. Geophys. Res., 82:3141-3152.

Chandrasekhar, S., 1960. Radiative transfer, Dover publications, New York.

Charney, J., W. Quirk, S. Chow, and J. Kornfield, 1977. A comparative study of the effects of surface albedo on drought in semi-arid regions, J. Atmos. Sci., 34:1366-1385.

Cooper, D. and G. Asrar, 1989. Evaluating atmospheric correction models for retrieving surface temperatures from the AVHRR over a tallgrass prairie, Remote Sensing Environ., 27:93-102.

Dave, J., 1972. Development of programs for computing characteristics of ultraviolet radiation, Tech. Report, NAS5-21680, NASA/GSFC, Greenbelt, MD

Dave, J., 1978. Extensive datasets of the diffuse radiation in realistic atmospheric models with aerosols and common absorbing gases, Solar Energy, 21:361-369.

D'Almeida, G., 1986. A model for Saharan dust transport, J. Clim. Appl. Meteor., 25:903-916.

D'Almeida, G., 1987. On the variability of desert aerosol radiative characteristics, J. Geophys. Res., 92D3:3017-3026.

Dickinson, R., 1983. Land surface processes and climate-surface albedos and energy balance, Adv. Geophys., 25:305-353.

Frouin, R. and C. Gautier, 1987. Calibration and NOAA-7 AVHRR, GOES-5, and GOES-6 VISSR/VAS solar channels, Remote Sens. Environ., 22:73-102.

Fraser, R., R. Ferrare, S. Mattoo, and Y. Kaufman, 1987. Algorithm for atmospheric corrections of aircraft and satellite imagery acquired during FIFE, Internal Report, Code 613, NASA/GSFC, Greenbelt, MD

Gausman, H., 1985. Plant leaf optical properties in visible in near-IR light, Texas Tech Report No. 29, Lubbock, Tx

Goward, S., C. Tucker, and D. Dye, 1986. N. American vegetation patterns in Africa using satellite data, Int. J. Remote Sensing, 7(11):1583-1608.

Grant, L., 1987. Diffuse and specular characteristics of leaf reflectance, 22:309-322.

Gutman, G., D. Tarpley, and G. Ohring, 1987. Cloud screening for determination of land surface characteristics in a reduced resolution satellite data set, Int. J. Remote Sensing, 8:859-870.

Holben, B., Y. Kaufman, and J. Kendall, 1989. NOAA-11 AVHRR visible and near-IR inflight calibration, Int. J. Remote Sensing, in press.

Holben, B., T. Eck, and R. Fraser, 1989. Temporal and spatial variability of aerosol optical depth in the Sahel region, Int. J. Remote Sensing, in press.

Holben, B. and T. Eck, 1989. Precipitable water in the Sahel measured using Sun photometry, Agriculture and Forest Meteorology, in press.

Justice, C., and P. Hiernauz, 1986. Monitoring the grasslands of the Sahel using NOAA AVHRR data: Niger 1983, Int. J. Remote Sensing, 7(11):1475-1498.

Kanamitsu, M., and T. Krishnamurti, 1978. Northern summer tropical circulations during drought and normal rainfall months, Mon. Wea. Rev., 106:331-347.

Kidwell, K., 1986. NOAA Polar orbiter data users guide, NOAA Environmental Data on Information Service, National Climate Data Center, U.S. Department of Commerce, Washington, D.C.

Kimes, D. and P. Sellers, 1985. Inferring hemispherical reflectance of the Earth's surface for global energy budgets from remotely sensed nadir or directional radiance values, Remote Sensing Environ., 18:205-223.

Kimes, D., J. Norman, C. Walthall, 1985. Modeling the radiant transfer of sparse vegetation canopies, IEEE Trans. Geosci. Remote Sensing, GE-23(5):695-704.

Kneizys, F., E. Shettle, W. Gallery, J. Chetwynd, L. Abreu, J. Selby, S. Clough, and R. Fenn, 1983. Atmospheric transmittance/radiance: Computer Code Lowtran 6, AFGL-TR-83-0187, Environmental Research Paper, 846, Hanscom AFB, Mass.

Labovitz, M., D. Toll, and R. Kennard, 1982. Preliminary evidence for the influence of physiography and scale upon the autocorrelation function of remotely sensed data, Int. J. Remote Sensing, 3:13.

Lamb, P., 1978. Large scale tropical Atlantic surface circulation patterns associated with the sub-Saharan weather anomalies, Tellus, 30:240-251.

Malila, W., G. Suits, T. Seller, 1987. Analysis of satellite data radiometry, ERIM Final Report 197000-2-F.

Monad, T., 1986. The Sahel zone north of the equator, in M. Evenari, I. Nuy-Meir, and D. Goodal, Ecosystems of the world 12b, Hot deserts and arid shrublands, Elsevier, NY, 203-244.

McClatchey, R., R. Fenn, J. Selby, F. Voltz, and J. Garing, 1971. Optical properties of the atmosphere, AFGRL, 71-0279, Environmental Research Paper, 354, Hanscom AFB, Mass.

Motha, R., S. Leduc, L. Steuaert, C. Sakamoto, and N. Strommen, 1980. Precipitation patterns in West Africa, Mon. Wea. Review, 108:1567-1578.

Mohamed, A., and J.-P. Frangi, 1983. Humidity and turbidity parameters in Sahel: A case study for Niamey, Niger, J. Climate Appl. Meteorol., 22:1820-1824.

Neckel, H. and D. Labs, 1984. The solar radiation between 3300 and 12,500 A, Solar Physics, 90:205-258,

Nicholson, S., 1983. Rainfall and atmosphere circulation during drought periods and wetter years in West Africa, Mon. Wea. Rev., 109:2191-2207.

Middleton, B., D. Deering and S. Ahmad, 1987. Surface anisotropy and hemispheric reflectance of semi-arid plant communities, Remote Sensing Environ., xxx

Patterson, E., D. Gillette, and B. Stockton, 1977. Complex index of refraction between 300-700 nm for Saharan aerosols, J. Geophys. Res., 82:3153-3160/

Pinty, B., and G. Szechwch, 1985. A new technique of surface albedo inference from satellite, 24:741-750.

Price, J., 1985. On the analysis of thermal infrared imagery: the limited utility of apparent thermal inertia, Remote Sensing Environ., 18:59-73.

Price, J., 1987. Calibration of satellite radiometers and the comparison of vegetation indices, Remote Sensing Environ., 21:15-27.

Robinove, C., 1981. Arid land monitoring using Landsat albedo difference images, Remote Sensing Environ., 11:135-156.

Sellers, P., 1985. Canopy reflectance, photosynthesis and transpiration, Int. J. Remote Sensing, 6:1335-1372.

Sellers, P., 1987. Canopy reflectance, photosynthesis, and transpiration, II. The role of biophysics in the linearity of their interdependence, Remote Sensing Environ., 21:148-183.

Shibayama, M. and T. Askiyama, 1989. Seasonal visible, near-infrared and mid-infrared spectra of rice canopies i relation to LAI and above-ground dry biomass, Remote Sensing Environ., 27:119-128.

Strong, A., and E. P. McClain, 1984. Improved ocean surface temperatures from space-comparisons with drifting buoys, Bull. Am. Meteor. Soc., 65(2):138-142.

Sud, Y. and W. Smith, 1985. The influence of surface roughness of deserts on the July circulation - A numerical study, Boundary Layer Meteor., 33:1-35.

Taylor, x, 1979. xx

Toll, D., 1989. Solar surface albedo estimation using remotely sensed data, IGARSS89, 12th Canada Symp. Remote Sensing, Vancouver, Vol. 1, 177-180.

Thekaekara, M., 1973. Solar energy outside the Earth's atmosphere, Solar energy, 14:109-127.

Tucker, C., 1979. Red and photographic ir linear combinations for monitoring vegetation, Remote Sensing Environ., 7(11):1571-1581.

Tucker, C., 1986. Monitoring the grasslands of the Sahel, 1984-1987, Int. J. Remote Sensing, 7(11): 1571-1581.

Vukovich, F., D. Toll, and R. Murphy, 1987. Surface temperature and albedo relationships in Senegal derived from NOAA-7 satellite data, Remote Sensing Environ., 22:413-421.

Wolfe, W. and G. Zissis, eds., 1978. The infrared handbook, Office of Naval Research, Department of Navy, Arlington, VA.

TABLES

Table 1. Effective NOAA AVHRR solar irradiance ($W \cdot m^{-2} \cdot sr^{-1}$) for bands 1 and 2 from Thekaekara (1975) and Neckel and Labs (1984) solar irradiance data. Conversion factors from Thekaekara to Neckel and Labs.

	Channel (μm)	Thekaekara	Conversion	Neckel and Labs
NOAA-7	1- 0.571-0.686	53.79	1.054	56.67
	2- 0.713-0.986	80.60	1.023	82.48
NOAA-9	1- 0.570-0.699	57.56	1.059	60.93
	2- 0.714-0.983	78.23	1.022	79.94

Table 2. Pre-flight and post-flight calibration reflectance for Tambacounda, Senegal

	ρvis		ρnir		NDVI	
mm/dd/yy	pre	post	pre	post	pre	post
9/3/81	9.3	10.4	24.4	28.2	0.45	0.46
3/22/82	15.2	17.3	17.0	20.7	0.05	0.11
6/4/82	17.9	20.7	18.6	23.3	0.02	0.06
7/8/82	18.6	21.6	19.5	24.5	0.02	0.06
10/25/82	20.7	24.4	23.0	29.5	0.05	0.09
3/31/83	16.9	20.2	19.0	24.9	0.06	0.10
4/24/83	22.5	26.7	21.6	28.2	-0.02	0.03
5/11/83	27.7	32.7	25.3	32.9	0.08	0.13
8/17/83	16.4	19.8	19.9	26.5	0.09	0.14
3/1/84	17.2	19.1	21.1	25.8	0.05	0.15
3/9/84	16.5	21.2	18.3	24.9	0.05	0.08
3/16/84	19.4	24.1	20.6	28.1	0.03	0.08
6/30/84	16.6	21.0	20.0	27.5	0.09	0.13
7/17/84	17.2	21.8	27.3	30.5	0.13	0.17
8/3/85	14.6	15.8	23.9	28.1	0.24	0.28
8/25/85	11.8	13.3	22.4	30.4	0.31	0.39
9/10/85	13.5	14.8	28.5	33.6	0.36	0.39
10/27/85	11.6	12.9	13.9	16.9	0.09	0.13

Table 3. Latitudinally interpolated aerosol optical depth estimates for Tambacounda and Podor using Sun photometer data derived from Holben et al. (1989). The data were interpolated from monthly average aerosol optical depth estimates from (Agadez (16.58N 14.40W), Gao (16.16N 9.03W), Sevare (15.40N 4.01W) and Bamako (12.39N and 8.00W).

Tambacounda

	F	M	A	M	J	J	A	S	O
AVHRR Band 1[1]	0.37	0.43	0.64	0.78	0.89	0.49	0.44	0.49	0.49
AVHRR Band 2[2]	0.33	0.39	0.61	0.74	0.86	0.45	0.40	0.45	0.45
Sun Photometer[3]	0.33	0.39	0.60	0.74	0.86	0.45	0.40	0.45	0.45

Podor

	F	M	A	M	J	J	A	S	O
AVHRR Band 1	0.69	0.55	0.94	0.81	0.99	0.82	0.52	0.53	0.54
AVHRR Band 2	0.65	0.51	0.91	0.77	0.97	0.97	0.78	0.49	0.49
Sun Photometer	0.65	0.51	0.91	0.77	0.97	0.97	0.78	0.49	0.49

1- Band 1 band-pass represented by 0.639 μm (Fraser et al. 19xx).
2- Band 2 band-pass represented by 0.845 μm (Fraser et al. 19xx).
3- Sun Photometer measured at 0.875 μm.

Table 4. Comparison of Sun photometer network (τ'(seas)) versus surface visibility (τ'(vv)) derived optical depth estimates for Tambacounda.

	AVHRR BAND-1			AVHRR BAND-2		
mm/dd/yy	τ'(vv)	τ'(seas)	Change	τ'(vv)	τ'(seas)	Change
9/3/81	0.25	0.47	+0.12	0.22	0.44	+0.22
3/22/82	0.57	0.48	-0.09	0.53	0.44	-0.09
10/25/82	0.31	0.49	+0.18	0.28	0.46	+0.22
3/31/83	0.36	0.54	+0.18	0.32	0.50	+0.18
4/24/83	0.74	0.69	-0.05	0.70	0.65	-0.15
5/11/83	0.57	0.77	+0.20	0.53	0.73	+0.20
8/17/83	0.36	0.45	+0.09	0.32	0.41	+0.09
3/1/84	0.36	0.40	+0.04	0.35	0.37	+0.02
3/9/84	0.57	0.40	-0.17	0.51	0.40	-0.11
3/16/84	0.57	0.43	+0.32	0.53	0.40	-0.13
6/30/84	0.31	0.70	+0.39	0.28	0.66	+0.38
8/3/85	0.36	0.46	+0.10	0.32	0.42	+0.10
8/25/85	0.31	0.46	+0.15	0.28	0.43	+0.15
9/10/85	0.31	0.40	+0.09	0.27	0.45	+0.18
	----	----	-----	----	----	-----
average	0.46	0.54	+0.08	0.42	0.48	+0.06

Table 5. Proportion of NOAA AVHRR band pass to surface (E_{surf}) and exoatmospheric (E_0) irradiance by spectral region (i.e., visible and near-IR) and total solar. Model Dave (1978) Model 3 of gaseous absorption with light aerosol density for mid-latitude continental at 30° Sun zenith.

		Percent band-pass in visible (0.38-0.72 μm) for band-1, in near-ir (0.72-1.30), and total solar (0.33-3.0 μm) for bands 1&2 combined			
		% Sensed Vis or Near-IR		% Sensed in Total Solar	
NOAA-#	Channel (μm)	Surface	Exoatm.	Surface	Exoatm.
-7	1(.571-.686)	32.2	31.6	15.5	13.6
	2(.713-.986)	50.5	53.0	50.5	18.5
	1&2			34.0	26.1
-9	1(.570-.699)	34.1	33.6	16.4	14.4
	2(.714-.983)	53.1	54.3	53.1	19.5
	1&2			35.9	27.1

Table 6A. SW MID-IR Spectral Reflectance Estimate from Landsat TM analysis. October 23, 1986.

ANOVA STATISTICS

TM-Band# Indep. Var.	Offset	Slope	F-Value	R^2	C.V.
2	-.15(.00)	3.06(.03)	10308.6	0.82	8.44
3	-.02(.00)	2.18(.01)	23928.0	0.91	5.85
4	.23(.01)	0.10(.04)	6.3	0.00	19.71
NDVI	.48(.00)	-0.56(.00)	12596.8	0.84	7.77
(2&3)	-.08(.00)	2.92(.02)	18506.8	0.89	6.57
(2&3)&4	-	-	11277.5	0.91	6.01
(2&3),4&NDVI	-	-	8594.6	0.92	5.65

Pearson Correlation Coefficients

	2	3	4	(2&3)	(5&7)	NDVI
2	---					
3	.96	---				
4	.18	.61	---			
(2&3)	.98	.99	.09	---		
(5&7)	.90	.96	-.05	.94	---	
NDVI	-.83	-.93	.33	-.90	-.92	---

Table 6B. September 24, 1984 B- ANOVA STATISTICS

TM-Band# Indep. Var.	Offset	Slope	F-Value	R^2	C.V.
2	.14(.01)	1.40(.03)	1813.6	0.36	3.64
3	.08(.00)	1.31(.02)	6432.4	0.67	2.63
4	.06(.01)	1.31(.02)	4694.1	0.59	2.90
NDVI	.46(.00)	-.42(.03)	250.3	0.07	4.37
(2&3)	.08(.01)	1.48(.02)	3920.0	0.55	3.06
(2&3)&4	-	-	2607.1	0.62	2.81
(2&3),4,&NDVI	-	-	3589.2	0.77	2.18

Pearson Correlation Coefficients

	2	3	4	(2&3)	(5&7)	NDVI
2	---					
3	.88	---				
4	.79	.86	---			
(2&3)	.96	.97	.85	---		
(5&7)	.59	.81	.77	.74	---	
NDVI	-.34	-.46	.05	-.42	-.26	---

Table 6C. October 23, 1986 Pearson Correlation Coefficients

	(2&3)	4	(5&7)
2&3	---		
4	.83	---	
5&7	.80	.84	---

Table 7. Proportion of spectral Solar irradiance at surface by spectral region. Also given is percent diffuse to global. Analysis of Dave' (1978) atmosphere diffuse data set. Model 2 Gases with no aerosols. Model 3 gases plus low loading (τ'_a=0.09 @ .5 μm). Model 4 gases plus moderate aerosol loading (τ'_a=0.45 @ .5 μm). UV (0.31-0.38μm), VS(.38-.72μm), NR(.72-1.3μm) and MR(1.3-2.41μm).

	Sun Zenith Angle											
	0°				45°				70°			
Model 2	UV	VS	NR	MR	UV	VS	NR	MR	UV	VS	NR	MR
Direct	.039	.471	.385	.105	.031	.468	.395	.106	.014	.474	.431	.110
Diffuse	.313	.635	.051	.001	.288	.658	.054	.001	.220	.711	.850	.001
Global	.053	.479	.368	.100	.048	.480	.373	.098	.039	.460	.387	.097
Diff(%)	29.6	6.6	0.7	0.1	39.8	9.2	1.0	0.1	67.6	18.0	2.4	0.2
Model 3												
Direct	.038	.466	.386	.110	.031	.460	.397	.112	.014	.428	.434	.124
Diffuse	.154	.568	.242	.034	.142	.579	.245	.033	.111	.600	.257	.033
Global	.052	.478	.370	.101	.048	.478	.374	.099	.040	.474	.386	.099
Diff(%)	34.4	13.8	7.6	3.9	45.6	18.7	10.1	5.1	74.3	33.8	17.8	8.8
Model 4												
Direct	.037	.444	.390	.129	.029	.429	.402	.140	.012	.360	.434	.194
Diffuse	.077	.528	.340	.056	.070	.528	.345	.056	.058	.521	.359	.062
Global	.050	.472	.373	.104	.046	.471	.378	.105	.042	.464	.385	.108
Diff(%)	50.8	37.4	30.5	17.8	63.9	47.5	38.6	22.7	89.9	72.8	60.4	37.1

Table 8. Surface derived parameters for Tambacounda of visible reflectance (ρ_{vis}), near-IR reflectance (ρ_{nir}), solar albedo (ρ_s), surface temperature (T_s), and NDVI. Also included is the two week and four week antecedent precipitation for each date. Standard deviations are given within parentheses.

Date	ρ (vis)	ρ (nir)	ρ (sol)	NDVI	T(s)	Pp't 2-week	Pp't 4-week
9/3/81	9.0 (.4)	39.5 (.6)	30.0	0.63	305.3 (.8)	180.0	410.0
3/22/82	28.4 (1.0)	35.1 (1.5)	32.4	0.11	321.5 (xx)	0	0
6/4/82	26.8 (.8)	36.3 (.9)	31.7	0.15	328.5 (1.2)	0	0
7/8/82	27.2 (.6)	38.2 (.6)	32.7	0.17	317.1 (.8)	0	0
10/25/82	33.8 (.5)	49.8 (.5)	41.6	0.19	305.2 (2.5)	0	19.0
3/31/83	26.2 (.9)	36.6 (1.7)	31.5	0.17	326.1 (1.0)	0	0
4/24/83	44.5 (.4)	57.0 (.7)	51.5	0.13	314.9 (.7)	0	0
8/17/83	26.8 (1.9)	50.7 (2.3)	37.2	0.31	307.2 (5.2)	34.4	34.4
3/1/84	28.1 (.4)	40.3 (.5)	34.1	0.18	318.3 (1.6)	0	0
3/9/84	24.7 (.5)	44.0 (.9)	33.0	0.14	322.9 (.6)	0	0
3/16/84	40.1 (.5)	53.5 (.6)	42.7	0.14	324.1 (.5)	0	0
6/30/84	27.3 (2.3)	50.5 (2.1)	37.5	0.30	304.9 (1.3)	26.8	52.5
7/17/85	27.9 (1.0)	53.0 (0.8)	38.9	0.31	299.7 (.6)	18.8	45.6
8/3/85	21.8 (.9)	54.0 (.9)	35.1	0.42	295.5 (1.2)	44.1	52.1
8/25/85	15.9 (1.0)	48.7 (1.1)	29.2	0.43	299.8 (0.6)	26.0	79.0
9/10/85	19.3 (1.4)	60.1 (1.3)	35.7	0.51	304.9 (0.7)	84.4	105.3
10/27/85	20.7 (.8)	45.3 (1.3)	31.2	0.13	321.1 (0.8)	0	0

Table 9. Surface derived parameters for Podor of visible reflectance (ρ_{vis}), near-IR reflectance (ρ_{nir}), solar albedo (ρ_s), surface temperature (T_s), and NDVI. Also included is the two week and four week antecedent precipitation for each date. Standard deviations are given within parentheses.

Date	ρ (vis)	ρ (nir)	ρ (sol)	NDVI	T(s)	Pp't 2-week	Pp't 4-week
9/3/81	21.8 (.5)	51.2 (.7)	34.1	0.40	308.4 (.5)	63.0	71.4
3/22/82	49.5 (.6)	62.4 (.9)	56.9	0.11	321.7 (.8)	0	0
6/4/82	41.3 (.4)	51.3 (.5)	47.2	0.11	326.9 (.3)	0	0
7/8/82	46.4 (.2)	61.0 (.3)	54.3	0.13	319.8 (.6)	1	1
10/25/82	37.3 (.5)	41.0 (.8)	42.9	0.11	323.7 (.4)	0	5
3/31/83	33.1 (.5)	48.9 (.5)	40.8	0.19	325.5 (.6)	0	0
4/24/83	43.9 (.5)	53.4 (.6)	49.7	0.09	321.4 (.6)	0	0
3/1/84	34.7 (.4)	59.4 (.5)	45.9	0.26	313.5 (3.0)	0	0
3/9/84	37.8 (1.0)	46.8 (.9)	43.2	0.11	317.2 (0.9)	0	0
3/16/84	40.0 (.6)	55.0 (.8)	44.1	0.16	323.1 (0.4)	0	0
6/30/84	41.2 (.5)	59.2 (.6)	50.1	0.18	318.2 (.6)	36.0	36.0
7/17/85	40.4 (.5)	58.3 (.5)	49.3	0.18	316.1 (.3)	7.0	45.0
8/3/85	42.0 (1.0)	61.0 (1.3)	51.3	0.18	305.2 (.4)	9.0	47.0
8/25/85	42.5 (.9)	51.3 (1.1)	50.3	0.15	314.7 (.1)	0.8	1.8
9/10/85	38.0 (1.0)	61.2 (1.2)	48.7	0.23	320.3 (.7)	5.7	6.5
10/27/85	27.2 (.4)	40.0 (.6)	35.9	0.26	317.8 (.5)	7.0	7.0

TABLE 10: **Average values for the Radiation Parameters in Table 8 and 9 as a function of antecedent precipitation. Dry denotes no antecedent precipitation, and wet, the existence of antecedent precipitation.**

TAMBACOUNDA

	ρ_{vis}	ρ_{nir}	ρ_{sol}	NDVI	T(k)
DRY	0.296	0.390	0.356	0.150	321.6
WET	0.227	0.508	0.356	0.390	302.8
OVERALL	0.264	0.446	0.356	0.260	312.8

PODOR

	ρ_{vis}	ρ_{nir}	ρ_{sol}	NDVI	T(k)
DRY	0.400	0.461	0.469	0.140	321.3
WET	0.333	0.538	0.463	0.190	316.0
OVERALL	0.362	0.505	0.466	0.170	318.3

TABLE 11: **Average values for the visible and near infrared reflectance and albedo as a function of NDVI**

	TAMBACOUNDA			*PODOR*		
NDVI	ρ_{vis}	ρ_{nir}	ρ_{sol}	ρ_{vis}	ρ_{nir}	ρ_{sol}
< 0.200	0.301	0.436	0.362	0.412	0.541	0.483
≥ 0.200	0.211	0.509	0.348	0.304	0.530	0.412

Table 12. Pearson correlation coefficient (r) matrix for AVHRR surface parameters and antecedent precipitation for Tambacounda.

	1	2	3	4	5	6	7
1) ρvis	1						
2) ρnir	.25	1					
3) ρalb	.83	.64	1				
4) NDVI	-.80	.29	-.37	1			
5) T_{sur}	.32	-.57	-.11	-.67	1		
6) Pp't (2 wks)	-.67	.10	-.25	.85	-.49	1	
7) Pp't (4 wks)	-.65	-.02	-.27	.79	-.44	.97	1

Table 13. Pearson correlation coefficient matrix for AVHRR surface parameters and antecedent precipitation for Podor.

	1	2	3	4	5	6	7
1) ρvis	1						
2) ρnir	.58	1					
3) ρalb	.95	.79	1				
4) NDVI	-.82	-.02	-.62	1			
5) T_{sur}	.15	-.41	-.07	-.49	1		
6) Pp't (2 wks)	-.56	-.02	-.41	.72	-.53	1	
7) Pp't (4 wks)	-.64	-.14	-.52	.75	-.52	.88	1

Figure Captions

Figure 1. Water vapor optical depth plotted with ambient air temperature and dew point temperature for Tambacounda, Senegal.

Figure 2. Water vapor optical depth plotted with ambient air temperature and dew point temperature for Podor, Senegal.

Figure 3. Vertical atmospheric transmissivity plotted against horizontal surface visibility.

Figure 4. Typical green leaf optical properties.

Figure 5. Monthly estimates of precipitation (A), ambient air temperature (B), and lifting condensation level (C) for Tambacounda, Senegal.

Figure 6. Monthly estimates of precipitation (A), ambient air temperature (B), and lifting condensation level (C) for Podor, Senegal.

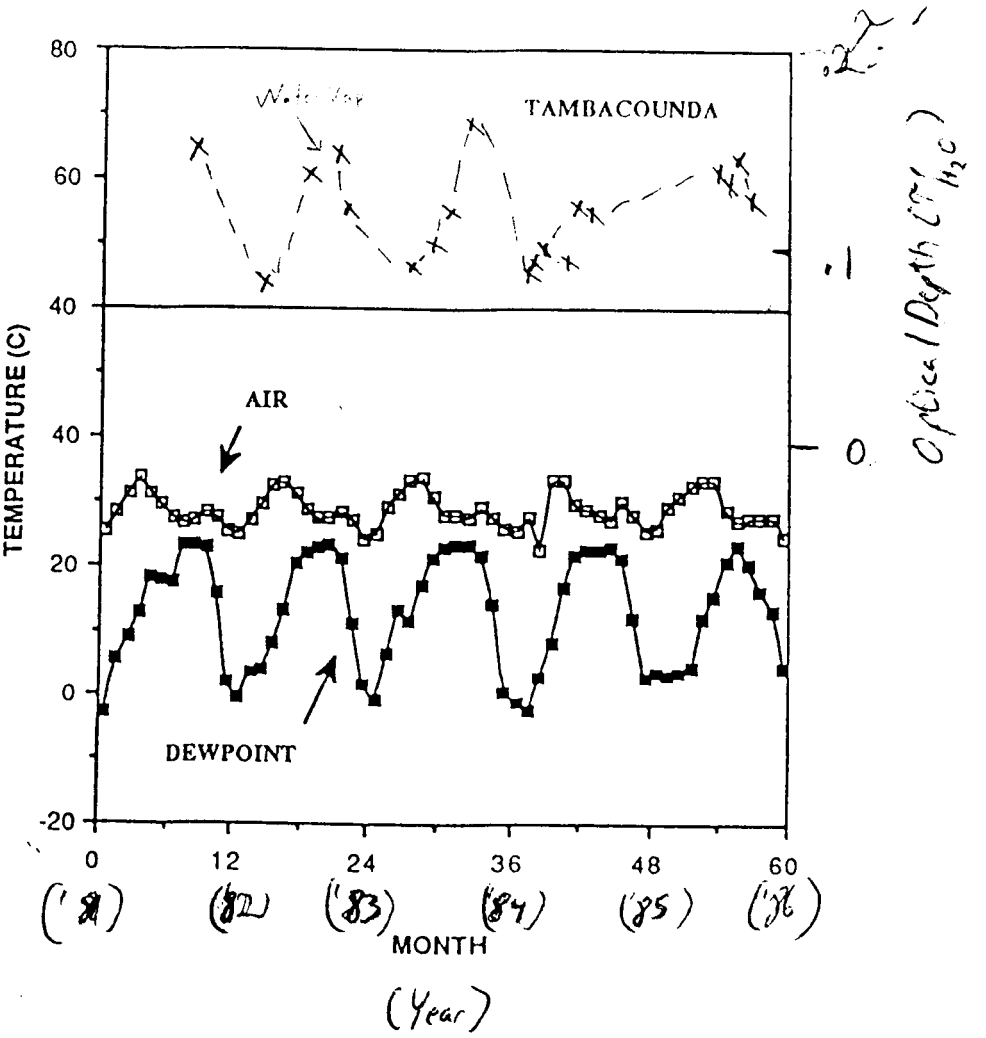

Figure 1

ORIGINAL PAGE IS
OF POOR QUALITY

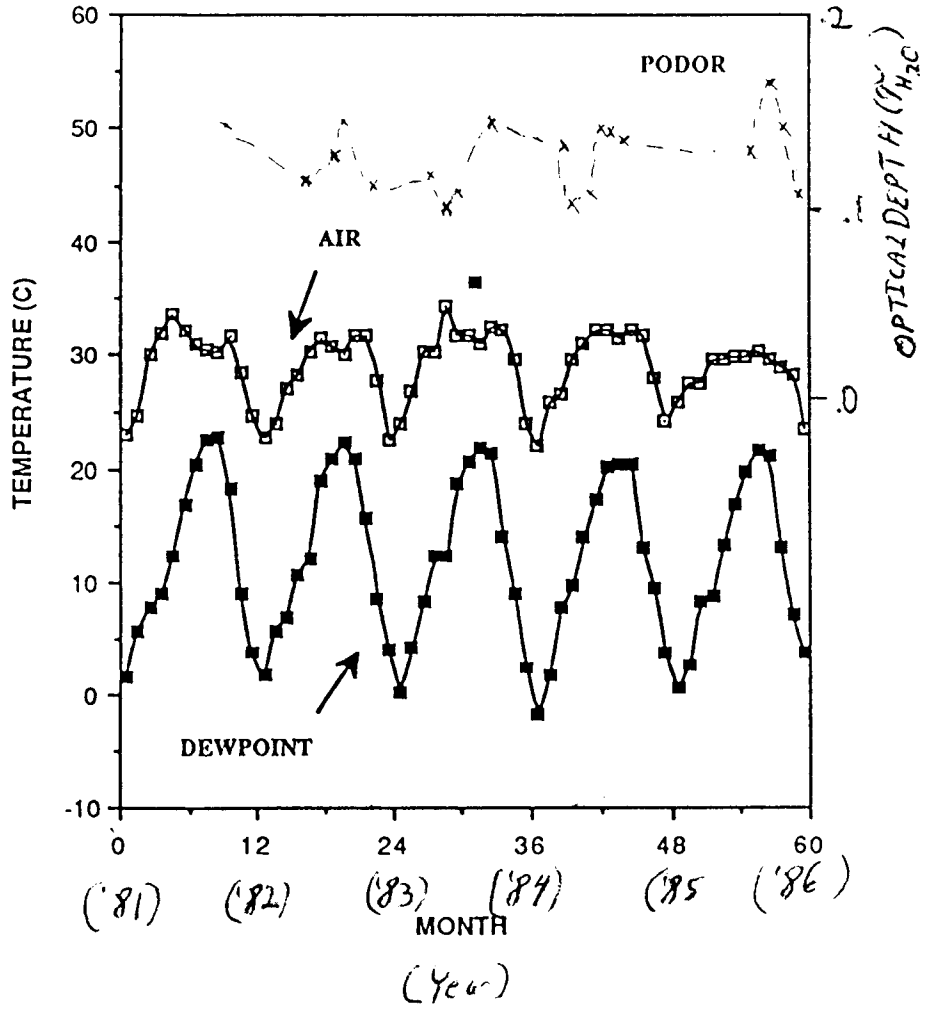

Fig. 2

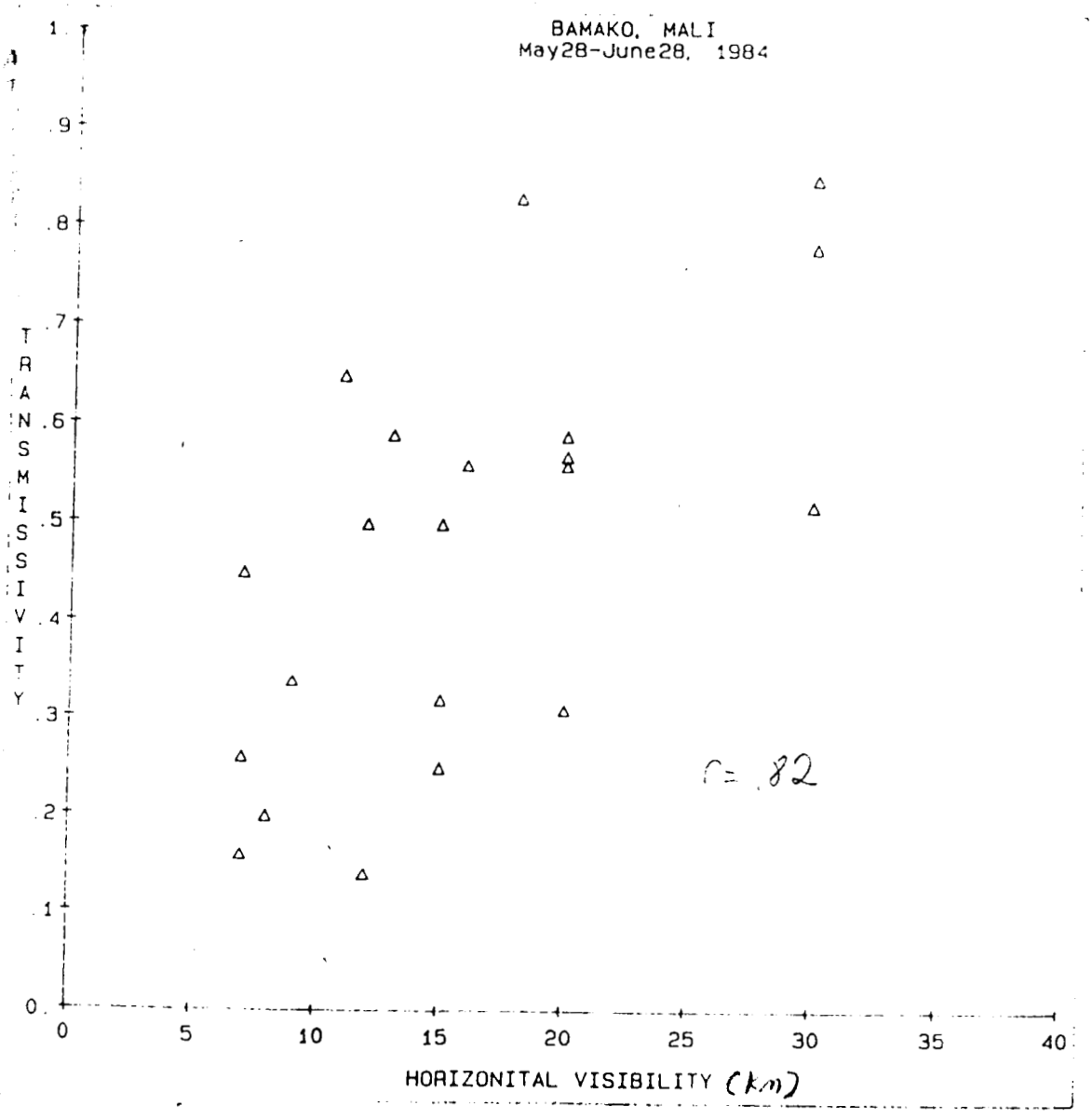

Fig 3

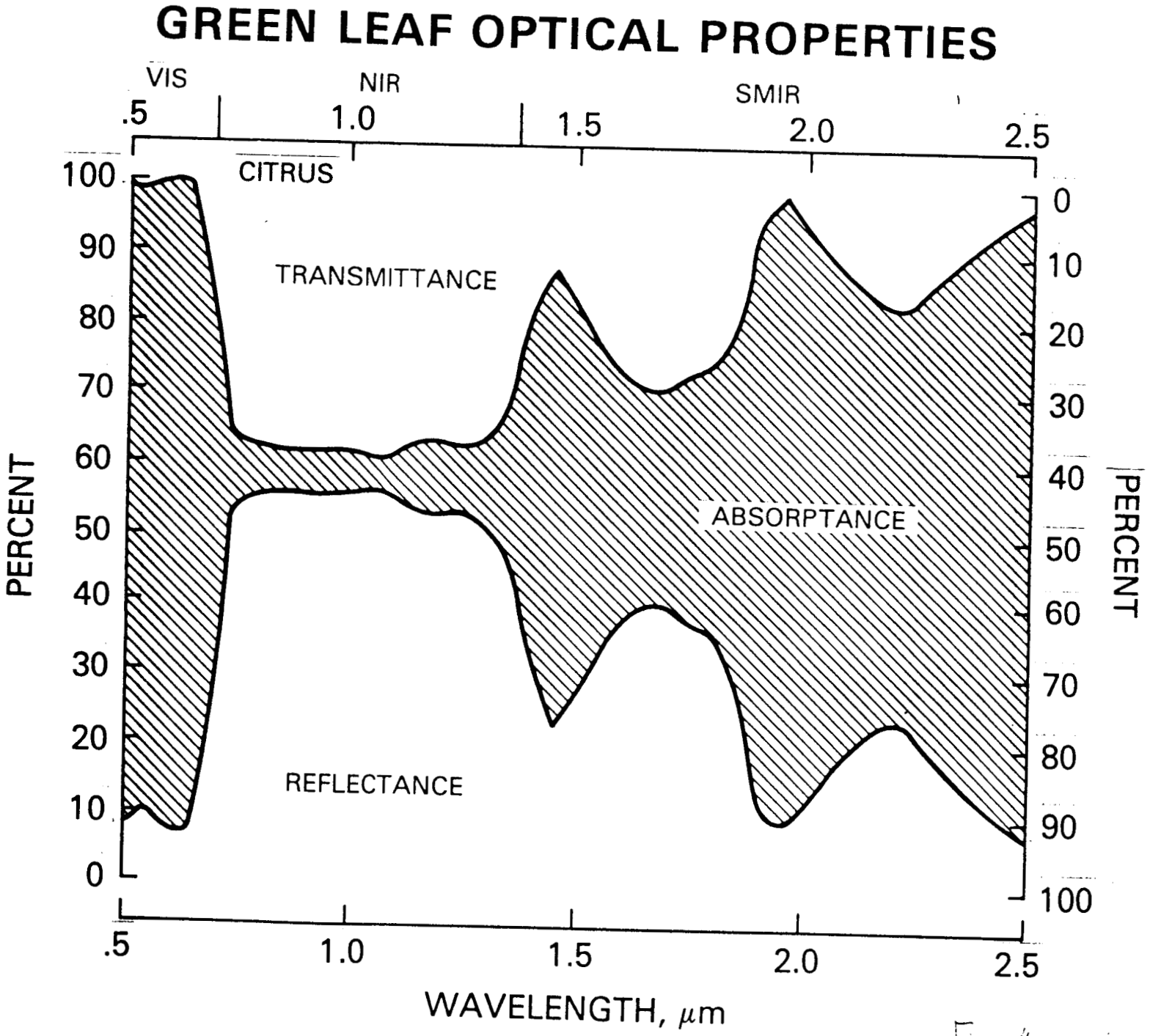
GREEN LEAF OPTICAL PROPERTIES
VIS
NIR
SMIR
.5
1.0
1.5
2.0
2.5
CITRUS
TRANSMITTANCE
ABSORPTANCE
REFLECTANCE
PERCENT
100
90
80
70
60
50
40
30
20
10
0
WAVELENGTH, μm

Figure 4

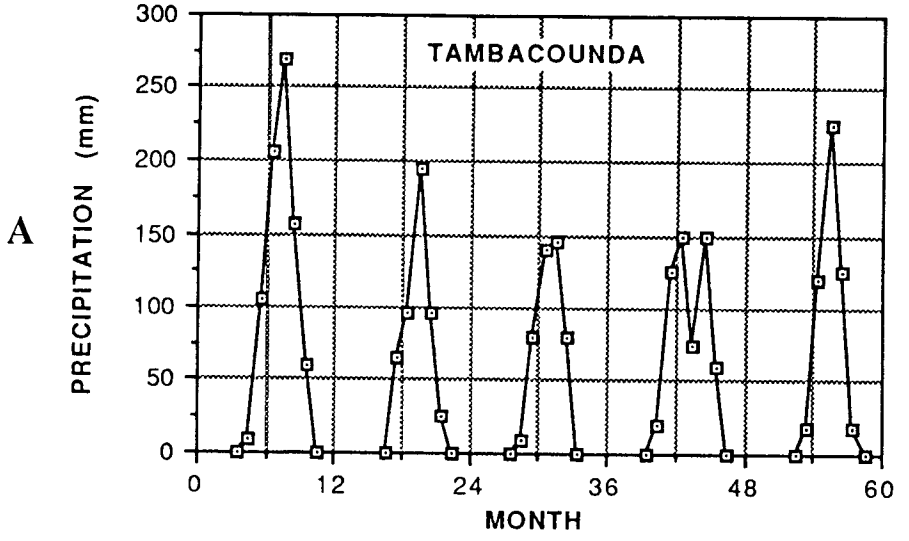
A
TAMBACOUNDA
PRECIPITATION (mm)
300
250
200
150
100
50
0
0
12
24
36
48
60
MONTH

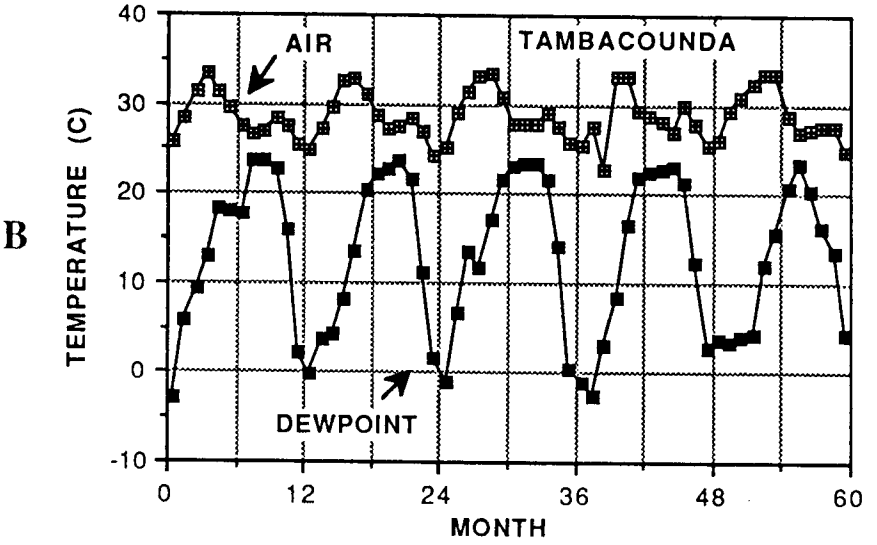
B
AIR
TAMBACOUNDA
TEMPERATURE (C)
40
30
20
10
0
-10
DEWPOINT
0
12
24
36
48
60
MONTH

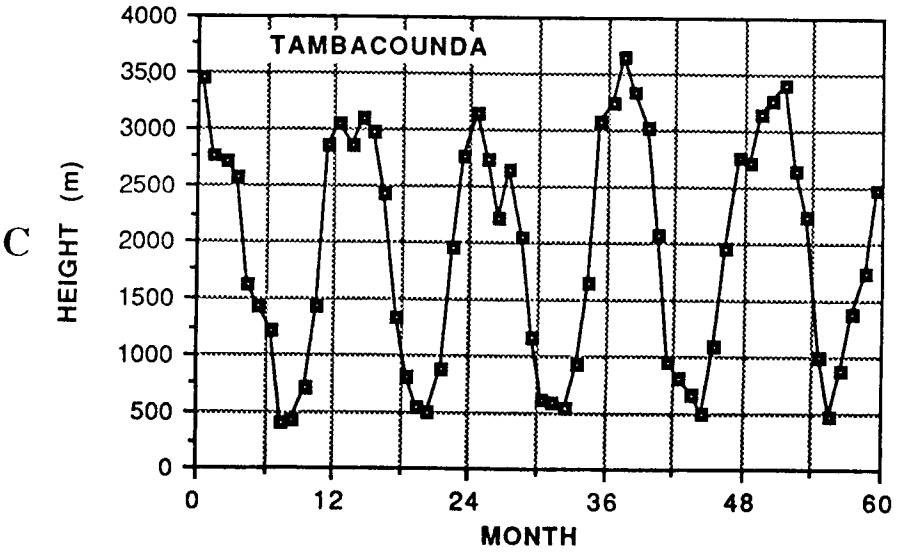
C
TAMBACOUNDA
HEIGHT (m)
4000
3500
3000
2500
2000
1500
1000
500
0
0
12
24
36
48
60
MONTH

Figure 5.

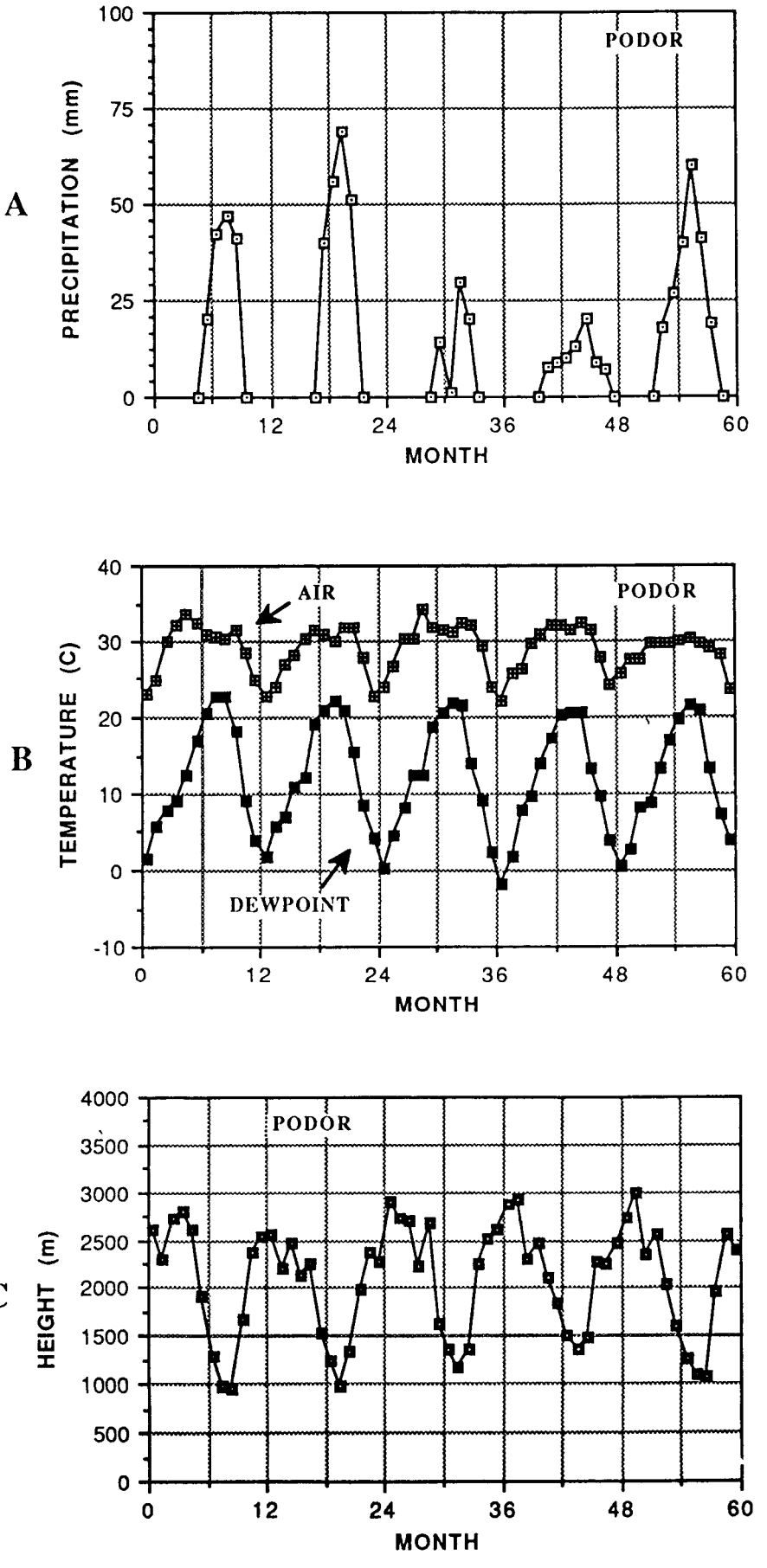
A
PODOR
PRECIPITATION (mm)
100
75
50
25
0
0
12
24
36
48
60
MONTH
B
AIR
PODOR
DEWPOINT
TEMPERATURE (C)
40
30
20
10
0
-10
0
12
24
36
48
60
MONTH
C
PODOR
HEIGHT (m)
4000
3500
3000
2500
2000
1500
1000
500
0
0
12
24
36
48
60
MONTH

Figure 6